Title
Persistent Charge-Density-Wave Order in Single-Layer TaSe2

Journal
Nano Letters, 18(2)

ISSN
1530-6984

Authors
Ryu, Hyejin
Chen, Yi
Kim, Heejung
et al.

Publication Date
2018-02-14

DOI
10.1021/acs.nanolett.7b03264

Peer reviewed

Persistent charge-density-wave order in single-layer $TaSe_2$

Hyejin Ryu[1,2,†,*], Yi Chen[3,†], Heejung Kim[4], Hsin-Zon Tsai[3], Shujie Tang[1,5], Juan Jiang[1], Franklin Liou[3], Salman Kahn[3], Caihong Jia[3, 6], Arash A. Omrani[3], Ji Hoon Shim[4,7], Zahid Hussain[1], Zhi-Xun Shen[5,8], Kyoo Kim[2,4], Byung Il Min[4], Choongyu Hwang[9], Michael F. Crommie[3, 10, 11], and Sung-Kwan Mo[1, *]

[1]*Advanced Light Source, Lawrence Berkeley National Laboratory, Berkeley, CA 94720, USA*

[2]*Max Planck POSTECH Center for Complex Phase Materials, Pohang University of Science and Technology, Pohang 37673, Korea*

[3]*Department of Physics, University of California, Berkeley, CA 94720, USA*

[4]*Department of Physics, Pohang University of Science and Technology, Pohang 37673, Korea*

[5]*Stanford Institute for Materials and Energy Sciences, SLAC National Accelerator Laboratory, Menlo Park, CA 94025, USA*

[6]*Henan Key Laboratory of Photovoltaic Materials and Laboratory of Low-dimensional Materials Science, Henan University, Kaifeng 475004, People's Republic of China*

[7]*Department of Chemistry and Division of Advanced Nuclear Engineering, Pohang University of Science and Technology, Pohang 37673, Korea*

[8]*Geballe Laboratory for Advanced Materials, Departments of Physics and Applied Physics, Stanford University, Stanford, CA 94305, USA*

[9]*Department of Physics, Pusan National University, Busan 46241, Korea*

[10]*Materials Sciences Division, Lawrence Berkeley National Laboratory, Berkeley, California 94720, USA*

[11]*Kavli Energy Nano Sciences Institute at the University of California Berkeley and the Lawrence Berkeley National Laboratory, Berkeley, California 94720, USA*

† These authors contributed equally to this work.

**e-mail: HRyu@lbl.gov, SKMo@lbl.gov*

Abstract

We present the electronic characterization of single-layer 1*H*-$TaSe_2$ grown by molecular beam epitaxy (MBE) using a combined angle-resolved photoemission spectroscopy (ARPES), scanning tunneling microscopy/spectroscopy (STM/STS), and density functional theory (DFT) calculations. We demonstrate that 3×3 CDW order persists despite distinct changes in the low energy electronic structure highlighted by the reduction in the number of bands crossing the Fermi energy (E_F) and the corresponding modification of Fermi surface (FS) topology. Enhanced spin-orbit coupling and lattice distortion in the single-layer limit play a crucial role in the formation of CDW order. Our findings provide a deeper understanding of the nature of CDW order in the 2D limit.

Table of Contents Graphic

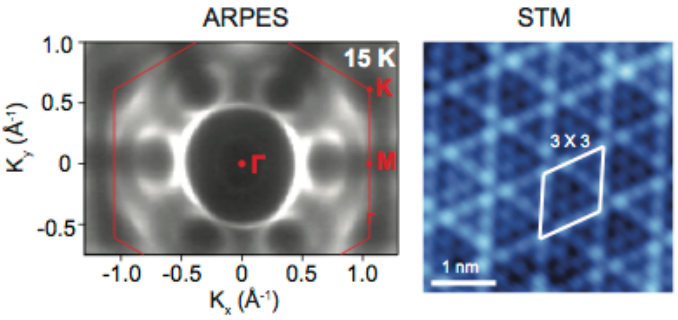

Keywords

Transition metal dichalcogenides, 2D materials, $TaSe_2$, charge density wave, CDW, MBE, ARPES, STM

2D materials, such as graphene, boron nitride, and TMDs host novel electrical, optical, and topological properties that differ from their bulk forms[1-3] and thus provide an ideal platform to study the effects of reduced dimensionality on the electronic ground states of many-body systems. In some TMDs, such as 2*H*-$TaSe_2$, 2*H*-$NbSe_2$, 1*T*-$TiSe_2$, and 1*T*-TaS_2, collective electronic phases such as CDW order and superconductivity can even coexist[4]. Reducing thickness down to a few layers allows interlayer interactions to be removed and provides vertical quantum confinement, enabling 2D collective interactions to be isolated and new quantum phases to arise. Such dimensional control provides a new means of probing the origin of CDW formation in metallic TMDs as well as the interplay of the CDW order with co-existing phases such as superconductivity[5].

Early work on bulk TMDs suggested the CDW instability arises from FS nesting, a straightforward extension of Peierls' scheme to 2D systems[6]. However, this description has been challenged by ARPES studies[7, 8] and electronic structure calculations[9], creating some controversy over the origin of the CDW in 2D TMD layers[4]. Alternative explanations, such as a saddle point (van Hove singularity) mechanism as well as electron-phonon coupling have been proposed[10]. While recent spectroscopic[11, 12], optical[13], and transport[14] studies on single-layer 1*H*-$NbSe_2$ were successful in observing significant suppression of superconductivity, they show contrasting results regarding CDW formation. The origin of this discrepancy is still debated.

2*H*-$TaSe_2$ provides an ideal material to investigate CDW formation in 2D TMDs without the complication of co-existing superconductivity, since superconductivity is

almost completely suppressed with a transition temperature of $T_C \sim 0.2$ K[15]. There exist two CDW transitions in the bulk form of $TaSe_2$, both having higher transition temperatures compared to other TMDs. A normal-to-incommensurate CDW transition occurs at $T_{N\text{-}IC} \sim 122$ K, followed by an incommensurate to commensurate CDW transition at $T_{IC\text{-}CC} \sim 90$ K.

Here we present combined ARPES/STM spectroscopy and DFT simulation indicating that when $TaSe_2$ thickness is reduced from bulk to single-layer the electronic band structure changes significantly due to a reduced number of bands crossing E_F in the normal state. Despite this evolution in electronic properties, however, the CDW remains unchanged. Reduced dimensionality appears to have no significant effect on either the 3×3 symmetry or $T_{N\text{-}IC}$. These results suggest that the CDW instability in single-layer 1*H*-$TaSe_2$ likely arises from electron-phonon coupling rather than FS nesting or a saddle point mechanism.

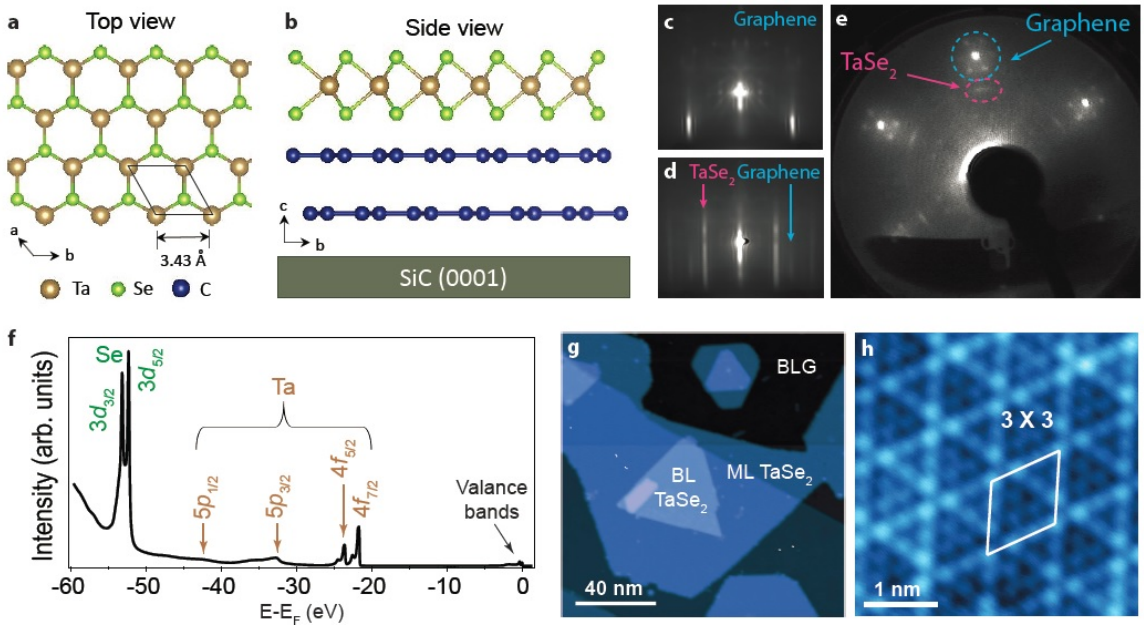

Figure 1. Growth of epitaxial single-layer 1*H*-$TaSe_2$ film. (a) Crystal structure of 1*H*-

$TaSe_2$ single-layer film on bilayer graphene over 6H-SiC(0001) from top view and (**b**) side view. (**c**) RHEED pattern of epitaxial bilayer graphene on 6H-SiC(0001) substrate and (**d**) 0.9 monolayer (ML, 0.9 ML means that 90% area of the substrate surface was covered by single-layer $TaSe_2$) 1*H*-$TaSe_2$ film. (**e**) LEED pattern of 0.9 ML 1*H*-$TaSe_2$ film. (**f**) Core-level spectra of 1*H*-$TaSe_2$ single-layer taken at 15 K with 80 eV photon energy. (**g**) Large-scale STM image of 0.9 ML 1*H*-$TaSe_2$/BLG (V_b = 1 V, I_t = 1 pA, T = 5 K). (**h**) Atomically resolved STM image of single-layer 1*H*-$TaSe_2$ shows 3x3 CDW order (V_b = 50 mV, I_t = 180 pA, T = 5 K).

Figs. 1a and b show the crystal structure of single-layer $TaSe_2$, which consists a layer of Ta atoms sandwiched between two layers of Se atoms in a trigonal prismatic coordination. The substrate is bilayer graphene (BLG) terminated 6H-SiC(0001). Sharp reflection high-energy electron diffraction (RHEED) patterns for single-layer film of $TaSe_2$ (Fig. 1d) indicate the high quality of films growing in a layer-by-layer mode. BLG diffraction spots observed in submonolayer $TaSe_2$ films (Fig. 1c) disappear when the $TaSe_2$ film coverage reaches a single layer. The low energy electron diffraction (LEED) pattern observed for single-layer $TaSe_2$ films (Fig. 1e) aligns well with the BLG diffraction pattern, indicating that $TaSe_2$ has the same lattice orientation as the substrate. The angle-integrated core level spectrum (Fig. 1f) displays sharp characteristic peaks for Ta and Se, demonstrating the purity of the $TaSe_2$ film as well as consistency with previous reports on bulk samples[16]. Fig. 1g shows a large scale STM image illustrating the typical morphology of the single-layer $TaSe_2$ films. A zoom-in of the STM topography obtained at 5 K (Fig. 1h) exhibits a clear 3×3 CDW superlattice, the same as seen in bulk $TaSe_2$ single crystals[15].

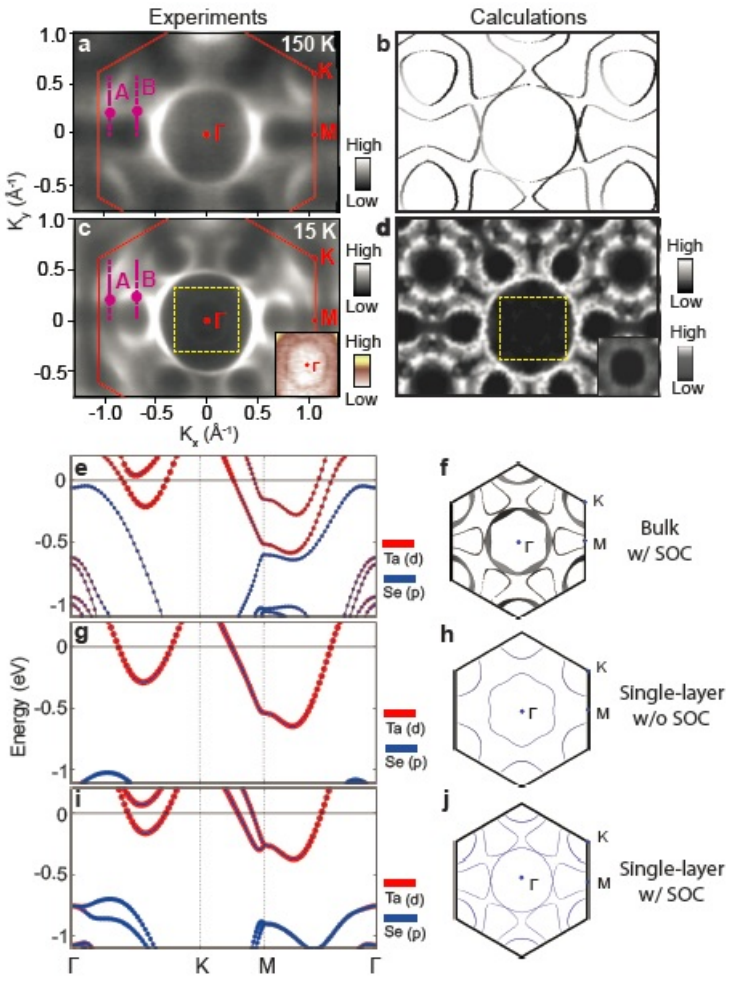

Figure 2. Electron band structure and Fermi surface of $TaSe_2$. (**a**) ARPES and (**b**) calculated Fermi surface (FS) map in normal state (150 K). (**c**) ARPES and (**d**) calculated FS in CDW state (15 K). Solid lines in **a** and **c** mark the 2D Brillouin zone of $TaSe_2$. Insets at the right bottom corner in (**c**) and (**d**) are the region marked by yellow dotted square around Γ with different color scale to display the low intensity features better. Calculated band structure and Fermi surface of normal-state $TaSe_2$ in its (**e**, **f**) bulk form with spin-orbit coupling (SOC), (**g, h**) single layer form without SOC, and (**i, j**) single layer form with SOC.

To investigate the electronic structure of single-layer $TaSe_2$, we first focus on the FS topology measured by *in situ* ARPES. Fig. 2 shows ARPES FS maps at temperatures above (Fig. 2a) and below (Fig. 2c) the CDW transition temperature, along with the simulated FS using DFT for the normal state (Fig. 2b) and CDW state (Fig. 2d). The calculated FS map

in CDW state is obtained from the unfolded band structures at chemical potential of -50 meV potentially due to the substrate effect. Since there is no detailed study on the interface structure between $TaSe_2$ and graphene, we tested the substrate effect using several possible arrangements in our calculations. This yields that the chemical potential is always shifted downwards consistently, with the amount of energy shift dependent on the assumed structures. The FS of single-layer $TaSe_2$ in the normal state (Figs. 2a and b) is similar to the FS of bulk $TaSe_2$[17, 18] in that it displays circular hole pockets around the Γ and K points and a dogbone-shaped electron pocket around the M points, but there is a significant difference. In contrast to bulk $TaSe_2$, the Γ point hole pocket and the M point electron pocket of single-layer $TaSe_2$ are not separated. This is due to a single band crossing E_F along the Γ-M direction, as a result of the reduced number of bands, from two to one, when $TaSe_2$ thickness is reduced to a single layer (Figs. 2e - j). The reduced number of bands crossing E_F and the resulting changes in FS are similar to what is seen for single-layer $NbSe_2$[11]. Our ARPES results are consistent with our calculation (Fig. 2b) as well as previous theoretical report[18].

The FS topology of $TaSe_2$ in the CDW state (Figs. 2c and d) also exhibits noticeable deviation from bulk $TaSe_2$. For example, the small triangular pocket seen previously around the K points is not observed in single-layer $TaSe_2$[17, 19]. Instead, a circular hole pocket is observed, similar to what is seen in the normal state. The absence of a triangular pocket around the K point is consistent with our calculated FS in the CDW state (Fig. 2d). Another important aspect of the FS topology in the CDW phase is that we clearly observe an extra

circular pocket around the Γ point (Inset of Fig. 2c) resulting from the folded bands, which has not been reported in the experimental FS of bulk $TaSe_2$[17, 19]. Our calculations suggest that enhanced amplitude of the lattice distortion in the CDW phase for the single-layer causes the absence of the triangular K pocket as well as the presence of band-folding around the Γ point (Inset of Fig. 2d).

We also find that spin-orbit coupling (SOC) plays a crucial role in determining the observed electronic structure and FS topology of single-layer $TaSe_2$. DFT calculations performed without (Figs. 2g and h) and with (Figs. 2i and j) SOC yields very different results. Without SOC only a single band crosses E_F along the Γ-K-M direction, very similar to what is seen for single-layer $NbSe_2$[11]. Inclusion of SOC, however, splits this band into two, thus separating the dogbone-shaped pocket around the M point. Our ARPES results are best explained by the calculation that includes SOC, implying that SOC plays a key role in determining the electronic structure of single-layer $TaSe_2$.

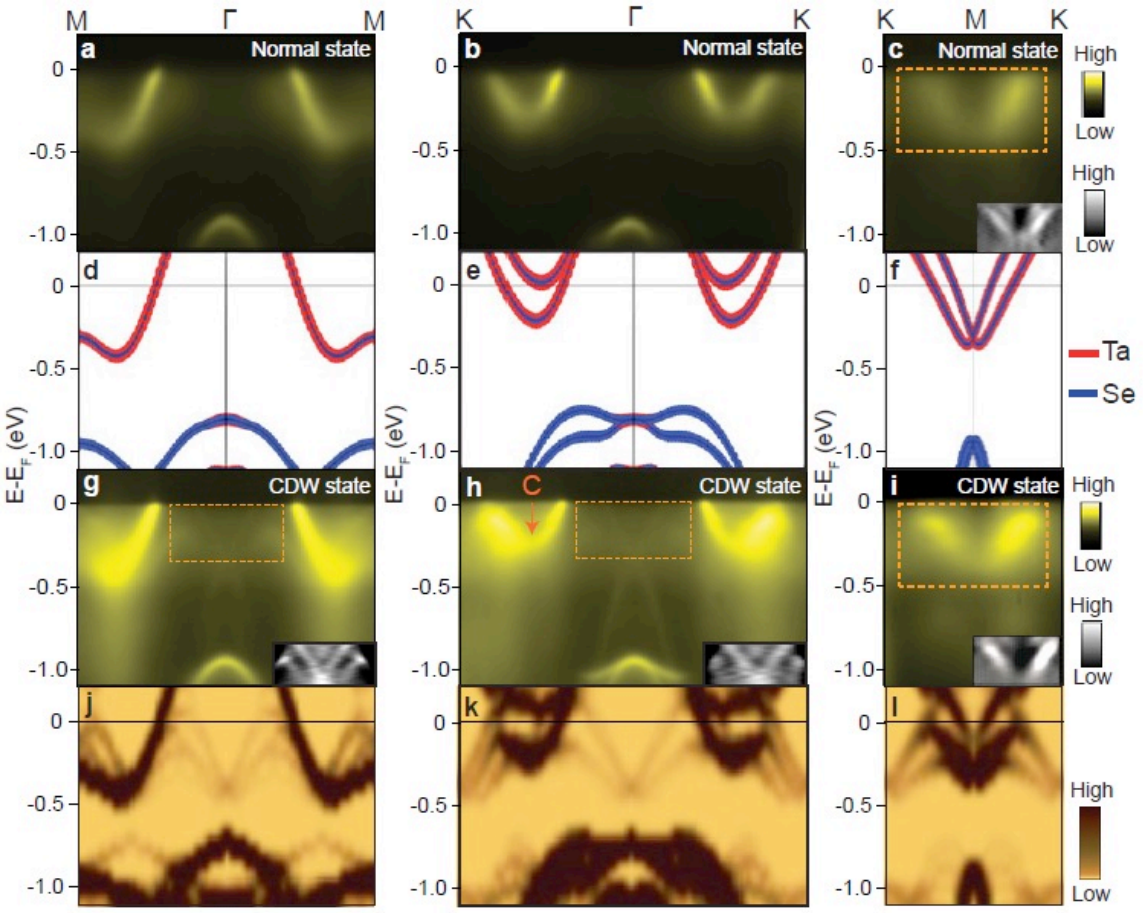

Figure 3. Electronic structure of single-layer $TaSe_2$ along high symmetry directions. ARPES spectra of normal-state (150 K) single-layer $TaSe_2$ along (**a**) Γ-M, (**b**) Γ-K, and (**c**) M-K directions compared with (**d-f**) calculated band structure. Red and blue bands in **d-f** denote Ta *d* and Se *p* orbital character, respectively. ARPES spectra of single-layer $TaSe_2$ in CDW state (T=15 K) along (**g**) Γ-M, (**h**) Γ-K, and (**i**) M-K directions compared to (**j-l**) calculated band structure. Insets at the right bottom corner in (**c**, **g-i**) are the second-derivative ARPES spectra of the region marked by yellow dotted square around Γ to enhance the visibility of low intensity features. Position C in **h** indicates saddle point along Γ-K direction located ~0.25 eV below E_F.

To further understand the electronic structure of single-layer $TaSe_2$, ARPES spectra along the high symmetry directions were measured at temperatures both above and below the CDW transition temperature (Fig. 3). The ARPES spectra in the normal state (Figs. 3a-c) are consistent with the reduced number of bands crossing E_F along the Γ-M direction,

and nicely match our calculated band structure (Figs. 3d-f). The features near $E < -1$ eV, which arises mainly from the Se *p* state, show some discrepancy between theory and experiment, likely due to the ill-description of electron correlations in LDA/GGA exchange correlation functional. The binding energy Se *p* band is indeed reasonably described by employing the mBJ method[20, 21] for bulk $TaSe_2$ (SI Fig. S2).

Fig. 3 also shows the measured ARPES band structures below the CDW transition temperature (Fig. 3g-i) as well as the DFT-calculated band structure including the 3×3 CDW-modulated supercell (Fig. 3j-l). The calculated bands are unfolded into a primitive cell from the fully relaxed 3×3×1 CDW-modulated supercell (see SI). The ARPES data and the calculated band structures show reasonable agreement in the dispersive band width and the binding energy of the Ta *d* orbital. The folded bands (i.e. the weak intensity spectra) around Γ and M for $E - E_F > -0.5$ eV are observed in ARPES and nicely reproduced in the calculation.

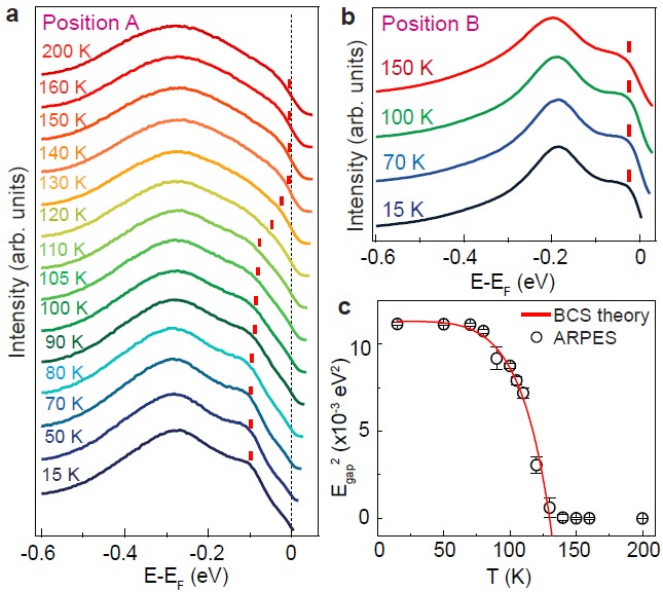

Figure 4. Temperature dependent band gap in single-layer $TaSe_2$ from ARPES. Temperature dependent EDCs at momentum positions (**a**) A and (**b**) B marked in Fig. 2**a**. Red tick marks indicate the peaks from which the gap is estimated. The EDCs have been divided by the Fermi-Dirac distribution function at corresponding temperatures to eliminate the effect of thermal broadening (see SI). **(c)** Band gap evolution with temperature shows BCS-like behavior.

To investigate the evolution of electronic structure as temperature is varied across the CDW transition temperature, temperature-dependent ARPES measurements were performed at the positions A and B of Fig. 2a. Energy gap values were determined by fitting peaks to the energy distribution curves (EDCs) and are indicated by red tick marks. The curves in Fig. 4a clearly show the temperature-dependent CDW gap opening at position A, whereas no gap is detected at position B. The single-layer CDW gap at T = 15 K is estimated to be 100 ± 13 meV, slightly larger than the bulk CDW gap measured previously to lie in the range 12 meV < E_{gap} < 80 meV via ARPES, STS and optical spectroscopy[4, 8, 17, 19]. The single-layer $TaSe_2$ coupling ratio, $2\Delta/k_B T_{N\text{-}IC}$, is thus seen to be 17.85, much larger than the value of 3.52 obtained by mean-field theory for weak-coupled CDW as well as the experimental values of 6.4 and 11 obtained for bulk $TaSe_2$[17, 19]. Fig. 4c shows the square of the measured CDW gap as a function of temperature, which is seen to closely follow a BCS gap equation[22]. The gap value decreases with increasing temperature until it reaches 0 at $T \sim 130$ K, thus yields a transition temperature of $T_{N\text{-}IC}$ = 130 ± 5 K for the transition from the normal phase to the ICDW phase of single-layer $TaSe_2$. This is slightly larger than the value of $T_{N\text{-}IC}$ = 122 K measured for bulk $TaSe_2$[23]. $TaSe_2$ thus exhibits the same general trend as $NbSe_2$ in that it displays a robust CDW transition even in single layer

limit[11].

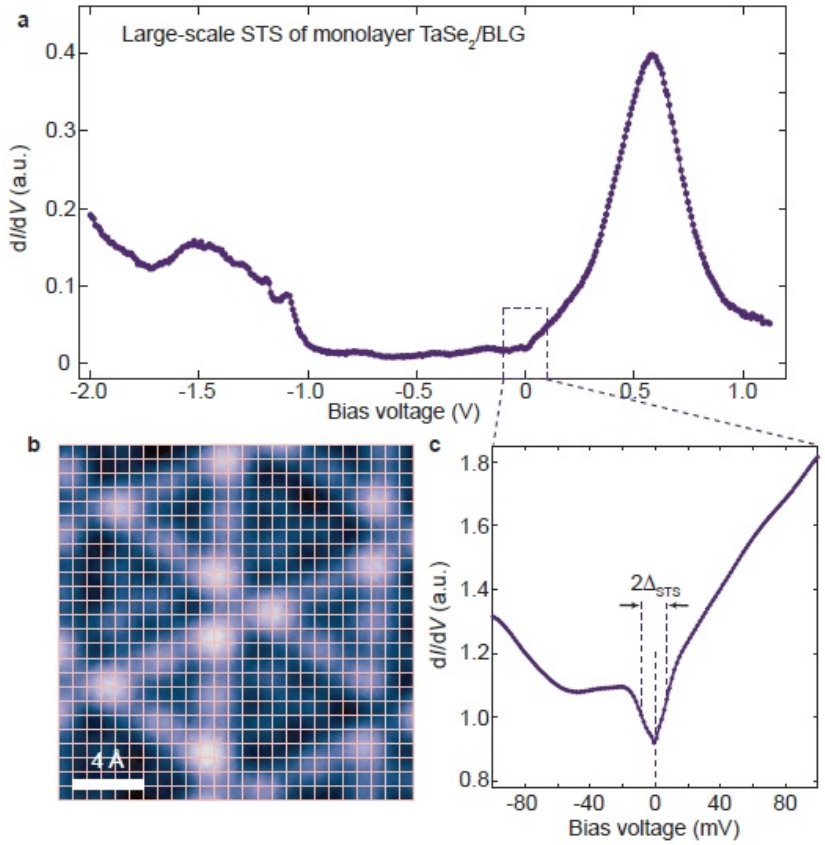

Figure 5. STS characterization of CDW state in single-layer $TaSe_2$. (a) Wide-bias STM dI/dV spectrum of single-layer $TaSe_2$ (f = 401 Hz, I_t = 10 pA, V_{RMS} = 10 mV, T = 5K). **(b)** Topographic image of single-layer $TaSe_2$ shows 25×25 grid where low-bias dI/dV spectra were obtained. **(c)** Low-bias dI/dV spectrum of single-layer $TaSe_2$ (average of spectra obtained over 25×25 grid shown in **(b)** (f = 401 Hz, I_t = 100 pA, V_{RMS} = 1 mV, T = 5K). STS partial gap width is $2\Delta_{STS}$ = 15.3 ± 3.5 meV (see SI).

STM/STS is complementary to ARPES in that it provides real-space identification of CDW order and related modification of low-energy electronic structure[24-26]. Fig. 5a shows a typical STM dI/dV spectrum of single-layer $TaSe_2$ acquired over a large bias range. In the filled state regime (V < 0) the spectrum is relatively flat and featureless until V = -1 V is reached, where a steep rise in dI/dV is seen as voltage is lowered. This is consistent with

our ARPES results since the local density of states (LDOS) for bands centered at *k*-values far from Γ (-0.5 eV < *E* < 0) is expected to be low, whereas the LDOS for bands centered at Γ (-0.5 eV < *E* < 0) is expected to be high[27, 28]. The dominant feature in the empty state regime is a broad peak centered at *E* ≈ -0.5 eV, likely due to a van Hove singularity at Γ in the conduction band[18]. A slight dip is seen at E_F. Overall, the wide-energy single-layer $TaSe_2$ spectrum of Fig. 5a is similar to what is seen for single-layer $NbSe_2$[3].

In order to better understand the low-energy electronic structure $TaSe_2$, we performed more highly-resolved d*I*/d*V* spectroscopy in the range -100 meV < *V* < +100 meV. d*I*/d*V* spectra were obtained on a 25×25 grid spread over a 20 Å × 20 Å region of the surface as shown in Fig. 5b. The average of theses spectra is shown in Fig. 5c (individual point spectra are shown in SI). A clear partial gap is observed that is centered at E_F (*V* = 0) and has width $2\Delta_{STS} = 15.3 \pm 3.5$ meV (see SI). A partially-opened STS gap is consistent with our ARPES measurements, as STS integrates over the contribution of all *k* points in reciprocal space, some of which are gapped (e.g., point A in Fig. 2a) and some of which are not (e.g., point B in Fig. 2a). In comparison to the CDW gap size of Δ = 100 ± 13 meV measured at the single *k* point A by ARPES, the reduced STS gap size suggest that the momentum-integrated STS spectrum is modified by the low-energy dispersion of in-gap states.

Our results allow us to draw some conclusions regarding the origin of the CDW instability of single-layer $TaSe_2$. First we note that FS nesting can be ruled out due to incompatibility between nesting ($\boldsymbol{q}_N$) and CDW ($\boldsymbol{q}_{CDW}$) wavevectors. Our results show that the CDW $\boldsymbol{q}$ for single-layer $TaSe_2$ is $\boldsymbol{q}_{CDW}$ = (1/3, 0, 0) whereas the geometric nesting of

the single-layer FS occurs at $\boldsymbol{q}_N$ = (1/3, 1/3, 0) (similar to bulk $TaSe_2$[9]). Single-layer $TaSe_2$, however, does exhibit gaps at different points along the FS, suggesting that FS nesting is not a necessary condition for CDW gap-opening.

Our data also indicates that a saddle point (van Hove singularity) mechanism[10] is not a suitable explanation for the origin of the CDW instability in $TaSe_2$. The saddle point mechanism predicts that the CDW gap will be centered at the saddle point along Γ-K (point C in Fig. 3h) which is located ~0.25 eV below E_F. However, our spectroscopic results indicate that the CDW gap is centered at the Fermi level. Our DFT calculations, consistent with previous report[18], reveal that both electron-phonon coupling constant and electronic susceptibility in single-layer $TaSe_2$ are much enhanced at $\boldsymbol{q}_{CDW}$, suggesting that strong momentum-dependent electron-phonon coupling is the likely driving force of the CDW order.

In conclusion, we have explored how dimensionality affects the CDW instability and electronic structure of in $TaSe_2$. Although single-layer $TaSe_2$ films exhibit different electronic structure compared to bulk $TaSe_2$, the 3×3 CDW order remains unchanged from the bulk case. We find that SOC and enhanced lattice distortion play an important role in the electronic structure of single-layer $TaSe_2$. These results suggest that the electron-phonon coupling rather than Fermi surface nesting or a saddle-point-based mechanism is the origin of CDW order in this material class.

Experimental Section

Thin film growth and ARPES. 1*H*-$TaSe_2$ was grown by MBE (base pressure 2×10^{-10} Torr) on epitaxial BLG[29] on 6H-SiC(0001) and transferred directly into the ARPES analysis chamber (base pressure 3×10^{-11} Torr) for the measurement at the HERS endstation of Beamline 10.0.1, Advanced Light Source, Lawrence Berkeley National Laboratory. High purity Ta (99.9%) and Se (99.999%) were evaporated from an e-beam evaporator and a standard Knudsen cell, respectively, with flux ratio Ta:Se = 1:3 and substrate temperature 550 ℃. This yields the growth rate of ~20 min per single-layer monitored by *in-situ* RHEED. The ARPES system was equipped with a Scienta R4000 electron analyzer. The photon energy was set at 55 eV with energy and angular resolution of 25 meV and 0.1 degree, respectively. Se capping layers ~ 10 nm were deposited onto single-layer 1*H*-$TaSe_2$ film at room temperature to prevent the contamination during transport through air to the ultrahigh vacuum scanning tunneling microscopy (UHV-STM) chamber. Se capping layers were removed by annealing the sample to ~520 K overnight in the UHV STM system before the STM/STS measurement.

RHEED, LEED, and large scale STM measurements were performed on 0.9 ML $TaSe_2$ sample in order to display the nature of the growth by showing the regions in which graphene, monolayer $TaSe_2$, and bilayer $TaSe_2$ coexist. The actual ARPES measurements were performed on 0.7 ML $TaSe_2$, which allows us to obtain only monolayer and graphene signal, since bilayer $TaSe_2$ starts to grow after ~70% of the substrate area is covered by monolayer. The ARPES signal from graphene near Fermi energy is isolated around the K-points of graphene, which exist at larger momenta than the first Brillouin zone boundary

of $TaSe_2$. Therefore, the low energy electronic structures measured by ARPES from graphene and from $TaSe_2$ do not interfere each other, allowing us to obtain ARPES spectra only from $TaSe_2$.

STM/STS measurement: STM/STS measurements were performed using a commercial Omicron LT-STM/AFM under UHV conditions at $T = 5$ K with tungsten tips. STM topography was obtained in constant-current mode. STM tips were calibrated on a Au(111) surface by measuring the Au(111) Shockley surface state before all STS measurements. STS was performed under open feedback conditions by lock-in detection of an alternating-current tunnel current with a small bias modulation at 401 Hz added to the tunneling bias. WSxM software was used to process the STM images.

Electronic structure calculation. For density functional theory (DFT) band calculations, we employed the *ab-initio* full-potential method implemented in Wien2k. The Vienna ab-initio simulation package (VASP) was also used for the band-unfolding[30] and structural relaxation. The generalized-gradient approximation (GGA) was utilized for the exchange-correlation potential. The electronic charge density was evaluated up to the kinetic energy cut-off of 600 eV. The Brillouin-zone (BZ) integration for self-consistent calculations was carried out with 20×20×6 *k*-points. SOC was included in the second variation manner. The Hellmann-Feynman force scheme was used for structural optimization. For the single-layer calculations, the distance of the out-of-plane is fixed at $c = 15$ Å, much larger than its natural value, in order to isolate one layer from the adjacent layers.

Supporting Information

Electronic structure calculation, Single-layer TaSe2 STS gap determination, Single-layer TaSe2 ARPES bandgap determination, Mean field behavior of the temperature dependent gap

Acknowledgements

Thin film growth and ARPES performed at the ALS was supported by the Office of Basic Energy Sciences, US DOE, under contract No. DE-AC02-05CH11231. Scanning probe measurements were supported by the VdW Heterostructure program (KCWF16) funded by the Office of Basic Energy Sciences, US DOE, under Contract No. DE-AC02-05CH11231 (STM spectroscopy), as well as by National Science Foundation award EFMA-1542741 (surface preparation). Support was also received from the Max Planck POSTECH center, supported by the NRF of Korea under project No. NRF-2011-0031558 (band structure calculation) and project No. 2015R1C1A1A01053065 (Fermi surface analysis). Surface analysis performed at the SIMES and Stanford University was supported by the Office of Basic Energy Sciences, US DOE, under contract No. DE-AC02-76SF00515. S. T. acknowledges the support by CPSF-CAS Joint Foundation for Excellent Postdoctoral Fellows. K. K. acknowledges the support by NRF of Korea under project No. 2016R1D1A1B02008461 and Max-Plank POSTECH center Research Initiative under grant No. 2016K1A4A4A01922028. B. I. M. acknowledges the support by NRF of Korea

under project No. 2015R1A2A1A15053564.

References

(1) Mannix, A. J.; Kiraly, B.; Hersam, M. C.; Guisinger, N. P. *Nature Reviews Chemistry* **2017,** 1, 0014.

(2) Chhowalla, M.; Jena, D.; Zhang, H. *Nature Reviews Materials* **2016,** 1, 16052.

(3) Novoselov, K. S.; Mishchenko, A.; Carvalho, A.; Castro Neto, A. H. *Science* **2016,** 353 (6298).

(4) Rossnagel, K. *J. Phys.: Condens. Matter* **2011,** 23 (21), 213001.

(5) Castro Neto, A. H. *Phys. Rev. Lett.* **2001,** 86 (19), 4382-4385.

(6) Grüner, G. *Reviews of Modern Physics* **1988,** 60 (4), 1129-1181.

(7) Arguello, C. J.; Rosenthal, E. P.; Andrade, E. F.; Jin, W.; Yeh, P. C.; Zaki, N.; Jia, S.; Cava, R. J.; Fernandes, R. M.; Millis, A. J.; Valla, T.; Osgood, R. M.; Pasupathy, A. N. *Phys. Rev. Lett.* **2015,** 114 (3), 037001.

(8) Laverock, J.; Newby, D.; Abreu, E.; Averitt, R.; Smith, K. E.; Singh, R. P.; Balakrishnan, G.; Adell, J.; Balasubramanian, T. *Phys. Rev. B* **2013,** 88 (3), 035108.

(9) Johannes, M. D.; Mazin, I. I. *Phys. Rev. B* **2008,** 77 (16), 165135.

(10) Johannes, M. D.; Mazin, I. I.; Howells, C. A. *Phys. Rev. B* **2006,** 73 (20), 205102.

(11) Ugeda, M. M.; Bradley, A. J.; Zhang, Y.; Onishi, S.; Chen, Y.; Ruan, W.; Ojeda-

Aristizabal, C.; Ryu, H.; Edmonds, M. T.; Tsai, H.-Z.; Riss, A.; Mo, S.-K.; Lee, D.; Zettl, A.; Hussain, Z.; Shen, Z.-X.; Crommie, M. F. *Nature Phys.* **2016,** 12 (1), 92-97.

(12) Bawden, L.; Cooil, S. P.; Mazzola, F.; Riley, J. M.; Collins-McIntyre, L. J.; Sunko, V.; Hunvik, K. W. B.; Leandersson, M.; Polley, C. M.; Balasubramanian, T.; Kim, T. K.; Hoesch, M.; Wells, J. W.; Balakrishnan, G.; Bahramy, M. S.; King, P. D. C. *Nature Comm.* **2016,** 7, 11711.

(13) Xi, X.; Zhao, L.; Wang, Z.; Berger, H.; Forró, L.; Shan, J.; Mak, K. F. *Nature Nanotech.* **2015,** 10 (9), 765-769.

(14) Xi, X.; Wang, Z.; Zhao, W.; Park, J.-H.; Law, K. T.; Berger, H.; Forro, L.; Shan, J.; Mak, K. F. *Nature Phys.* **2016,** 12 (2), 139-143.

(15) Kumakura, T.; Tan, H.; Handa, T.; Morishita, M.; Fukuyama, H. *Czech J. Phys.* **1996,** 46 (5), 2611-2612.

(16) Brauer, H. E.; Starnberg, H. I.; Holleboom, L. J.; Hughes, H. P.; Strocov, V. N. *J. Phys.: Condens. Matter* **2001,** 13 (44), 9879.

(17) Borisenko, S. V.; Kordyuk, A. A.; Yaresko, A. N.; Zabolotnyy, V. B.; Inosov, D. S.; Schuster, R.; Büchner, B.; Weber, R.; Follath, R.; Patthey, L.; Berger, H. *Phys. Rev. Lett.* **2008,** 100 (19), 196402.

(18) Ge, Y.; Liu, A. Y. *Phys. Rev. B* **2012,** 86 (10), 104101.

(19) Rossnagel, K.; Rotenberg, E.; Koh, H.; Smith, N. V.; Kipp, L. *Phys. Rev. B* **2005,** 72 (12), 121103.

(20) Tran, F.; Blaha, P. *Phys. Rev. Lett.* **2009,** 102 (22), 226401.

(21) Becke, A. D.; Johnson, E. R. *The Journal of Chemical Physics* **2006,** 124 (22), 221101.

(22) Chen, P.; Chan, Y. H.; Fang, X. Y.; Zhang, Y.; Chou, M. Y.; Mo, S. K.; Hussain, Z.; Fedorov, A. V.; Chiang, T. C. *Nature Comm.* **2015,** 6, 8943.

(23) Moncton, D. E.; Axe, J. D.; DiSalvo, F. J. *Phys. Rev. Lett.* **1975,** 34 (12), 734-737.

(24) Soumyanarayanan, A.; Yee, M. M.; He, Y.; van Wezel, J.; Rahn, D. J.; Rossnagel, K.; Hudson, E. W.; Norman, M. R.; Hoffman, J. E. *Proceedings of the National Academy of Sciences* **2013,** 110 (5), 1623-1627.

(25) Coleman, R. V.; Giambattista, B.; Hansma, P. K.; Johnson, A.; McNairy, W. W.; Slough, C. G. *Adv. Phys.* **1988,** 37 (6), 559-644.

(26) Qin, S.; Kim, J.; Niu, Q.; Shih, C.-K. *Science* **2009,** 324 (5932), 1314.

(27) Zhang, Y.; Brar, V. W.; Wang, F.; Girit, C.; Yayon, Y.; Panlasigui, M.; Zettl, A.; Crommie, M. F. *Nature Phys.* **2008,** 4 (8), 627-630.

(28) Tersoff, J.; Hamann, D. R. *Phys. Rev. Lett.* **1983,** 50 (25), 1998-2001.

(29) Qingyan, W.; Wenhao, Z.; Lili, W.; Ke, H.; Xucun, M.; Qikun, X. *J. Phys.: Condens. Matter* **2013,** 25 (9), 095002.

(30) Ku, W.; Berlijn, T.; Lee, C.-C. *Phys. Rev. Lett.* **2010,** 104 (21), 216401.